

# Geomagnetic data from the GOCE satellite mission

I. Michaelis<sup>1</sup>, K. Styp-Rekowski<sup>2,1</sup>, J. Rauberg<sup>1</sup>, C. Stolle<sup>3</sup>, and M. Korte<sup>1</sup>

<sup>1</sup>Helmholtz Centre Potsdam, GFZ German Research Centre for Geosciences, Telegrafenberg, 14473

Potsdam, Germany, ingo.michaelis@gfz-potsdam.de.

<sup>2</sup>Technical University of Berlin, Electrical Engineering and Computer Science, Ernst-Reuter-Platz 7,

10587 Berlin, Germany

<sup>3</sup>Leibniz-Institut für Atmosphärenphysik e.V., an der Universität Rostock Schloßstraße 6, 18225

Kühlungsborn, Germany

## Abstract

The Gravity field and steady-state ocean circulation explorer (GOCE) is part of ESA's Earth Explorer Program. The satellite carries magnetometers that control the activity of magnetorquers for navigation of the satellite but are not dedicated as science instruments. However, intrinsic steady states of the instruments can be corrected by alignment and calibration, and artificial perturbations, e.g., from currents, can be removed by their characterisation correlated to housekeeping data. The leftover field then shows the natural evolution and variability of the Earth's magnetic field. This article describes the pre-processing of input data as well as calibration and characterisation steps performed on GOCE magnetic data, using a high precision magnetic field model as reference. For geomagnetic quiet times, the standard deviation of the residual is below 13 nT with a median residual of (11.7, 9.6, 10.4) nT for the three magnetic field components (x,y,z). For validation of the calibration and characterisation performance, we selected a geomagnetic storm event in March 2013. GOCE magnetic field data shows good agreement with results from a ground magnetic observation network. The GOCE mission overlaps with the dedicated magnetic field satellite mission CHAMP for a short time at the beginning of 2010, but does not overlap with the Swarm mission or any other mission flying at low altitude and carrying high-precision magnetometers. We expect calibrated GOCE magnetic field data to be useful for lithospheric modelling and filling the gap between the dedicated geomagnetic missions CHAMP and Swarm.

## Keywords

Earth's magnetic field, Geomagnetism, Ionospheric currents, Magnetospheric ring current, Satellite-based magnetometers, Platform magnetometers, GOCE

## Introduction

In the last two decades, low Earth orbiting (LEO) satellites have been in-orbit for accurate measurement of the geomagnetic field using dedicated instruments, e.g. missions like CHAMP (CHAMP 2019) and Swarm (Olsen et al. 2013). However, there is a temporal gap of about 3 years between these dedicated missions.

In addition, single missions can only provide limited coverage in local time at a given time. Enhancement of simultaneous local time coverage is given by multi-mission constellations. To this aim, magnetometer data from missions like CryoSat-2 (Olsen et al. 2020), GRACE (Olsen 2020), and GRACE-FO (Stolle et al. 2021) has been characterised and calibrated and made publicly available. Some of those missions can fill the gap between the high-level missions CHAMP and Swarm from 2010 to 2013, e.g. CryoSat-2 and GRACE, others can fill the gap in magnetic local time (MLT) distribution, e.g. GRACE-FO. An overview of scientific and platform magnetometer (PlatMag) missions is shown in Figure 1. Stolle et al. (2021) have shown that large scale field-aligned currents can be derived from GRACE-FO, as well as equatorial ring currents. The residuals of those datasets compared to high-level geomagnetic models like CHAOS-7 (Finlay et al. 2020) have been reduced to values well below 10 nT for geomagnetic quiet times, depending on the mission. This report introduces a calibrated magnetometer data set from the Gravity field and steady-state ocean circulation explorer (GOCE) mission, following a similar calibration and characterisation procedure of GRACE-FO (Stolle et al. 2021).

The GOCE mission has been operated by ESA. The primary objective of GOCE (Floberghagen et al. 2008, 2011; GOCE Flight Control Team 2014) was to obtain precise global and high-resolution models for both the static and the time-variable components of the Earth’s gravity field and geoid. GOCE has been successfully launched on 17 March 2009 and completed its mission on 11 November 2013. It was flying on a near-circular polar dawn-dusk orbit with an inclination of  $96.7^\circ$  and at a mean altitude of about 262 km, ([https://www.esa.int/Applications/Observing\\_the\\_Earth/FutureEO/GOCE/Facts\\_and\\_figures](https://www.esa.int/Applications/Observing_the_Earth/FutureEO/GOCE/Facts_and_figures)). A sketch of the satellite is shown in Figure 2 and a summary on the satellite’s orbits and body is available at ([https://www.esa.int/Enabling\\_Support/Operations/GOCE](https://www.esa.int/Enabling_Support/Operations/GOCE)). The GOCE satellite carries three magnetometers as part of its attitude and orbit control system mounted side-by-side displaced by 80 mm. The attitude is mainly controlled by ion thrusters for achieving a drag-free flight, and in addition magnetorquers are used. For magnetorquer activation, the actual magnetic field needs to be measured by magnetometers.

This article describes the original data, methods, and procedures of data processing, characterisation of disturbances, and calibration of instrument intrinsic parameters that are necessary to obtain scientifically useful magnetic field data from the GOCE platform magnetometers. We show the performance of the calibration and characterisation procedure by comparison to the CHAOS-7 field model, the illustration of Field Aligned Currents (FAC), and a comparison of the time series characterising a geomagnetic storm to

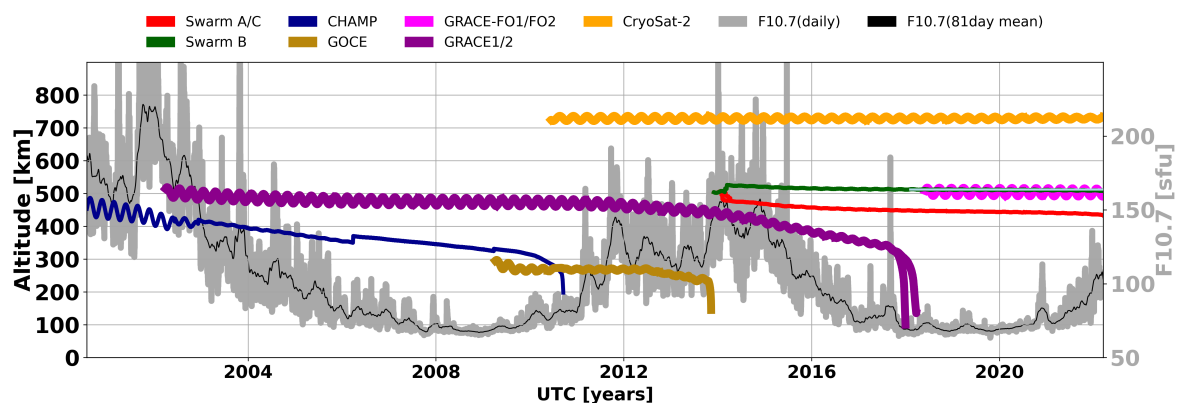


Figure 1. Overview of the two satellite missions dedicated to geomagnetic measurements CHAMP (blue line) and Swarm (red and green lines) and a selection of missions carrying platform magnetometers at their respective altitudes. Also shown is the F10.7 solar irradiation index as an indication of solar activity (grey with mean as black solid line, right axis).

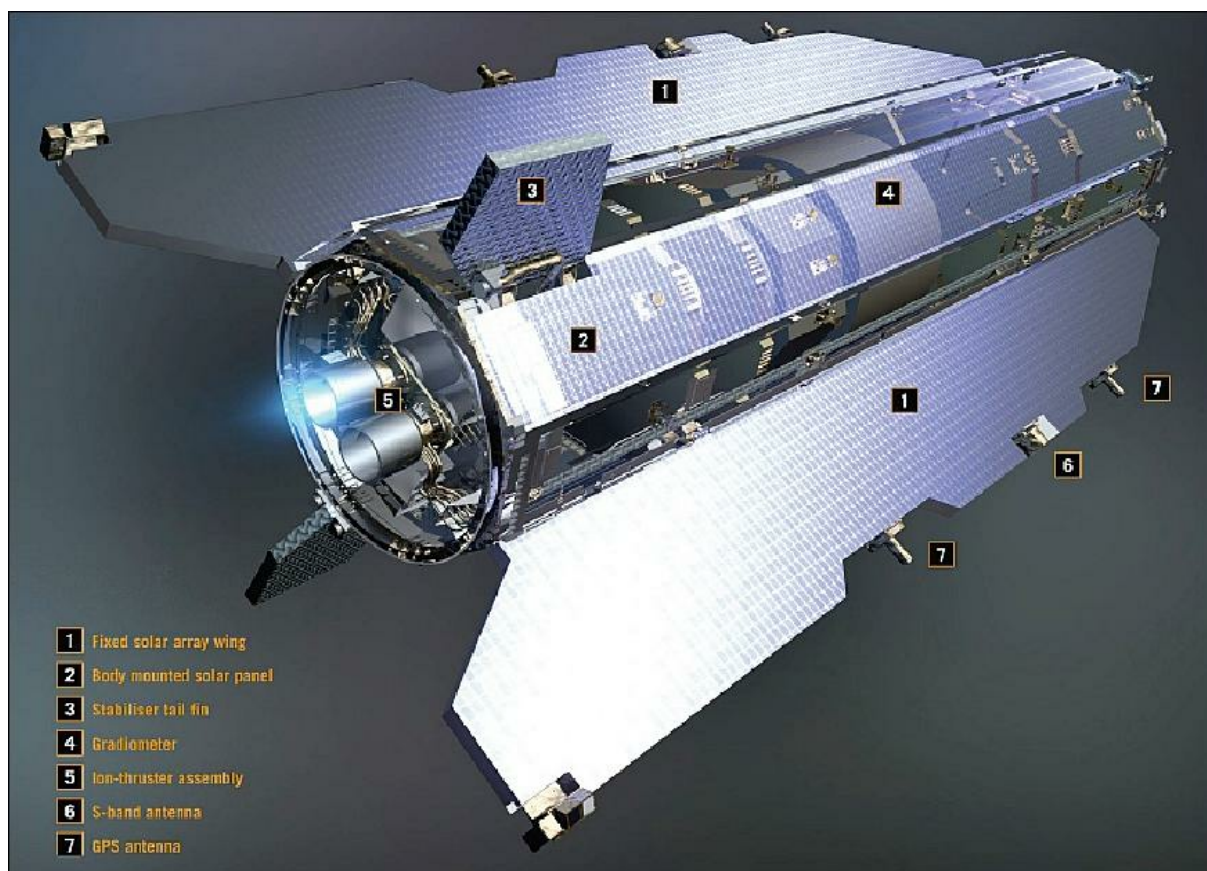


Figure 2. Schematic view of the GOCE satellite. (Credits: ESA)

the commonly used Dst index that is obtained from ground data. The processed magnetometer data described in this article is available at (Michaelis et al. 2022), for November 01, 2009 to September 30, 2013. The data published with this article is version 0205.

## Data sets and data pre-processing

### Instruments

As part of the Drag-free Attitude and Orbit Control System (DFACS), the GOCE satellite carries three active fluxgate magnetometers (MGM). The calibration and characterisation effort is part of Swarm DISC (Swarm DISC 2022). The PlatMag consortium within Swarm DISC decided to call magnetometer instrument reference frames MAG. Hence MGM will be further called MAG. Figure 3 shows the locations of the magnetometers onboard the satellite. The magnetometers are manufactured by Billingsley Aerospace&Defence and are of type TFM100S (Billingsley 2020). The measurement range is  $\pm 100 \mu\text{ T}$ , the root mean square noise level is  $\sim 12 \text{ pT}/\sqrt{\text{Hz}}$  and the resolution is  $3.05185 \text{ nT/bit}$ , (Kolkmeier et al 2008). The data is sampled at  $1/16 \text{ Hz}$ . The MAG data has been pre-calibrated achieving biases of less than  $500 \text{ nT}$ .

Magnetometer calibration further relies on attitude data derived from the Electrostatic Gravity Gradiometer (EGG) and three star cameras (STR) that are mounted on the shaded side of the satellite, shown in Figure 2. The strongest magnetic disturbance is expected from the magnetorquers (MTQ), although they are located as far away as possible from the magnetometers, see the overview of instrument location in Figure 3. Since magnetorquer currents are available, an almost full correction for them can be expected. GOCE’s whole telemetry of the satellite, including e.g. magnetometer, magnetorquer currents, attitude, solar array currents, battery currents, and magnetometer temperatures, is publicly available at <https://earth.esa.int/eogateway/missions/goce>. The telemetry datasets used for this article are listed in Table 1. GOCE L1b and L2 data is provided in zip files that contain ESA’s Earth Explorer Format (EEF) files for each L1b product. An overview of used products with given names, source, unit, and time resolution is listed in Table 1. Data stored as telemetry is given in zip files that contain ESA’s Earth Explorer header and data in ASCII. Time values are always handled as defined in the EEF. The dataset with the highest quality of input datasets is the attitude information since it relies on the main instrument of the mission. An interpolation may add numerical noise. Therefore it makes sense to use timestamps from the attitude dataset as reference for creating a series of timestamps. The timestamps

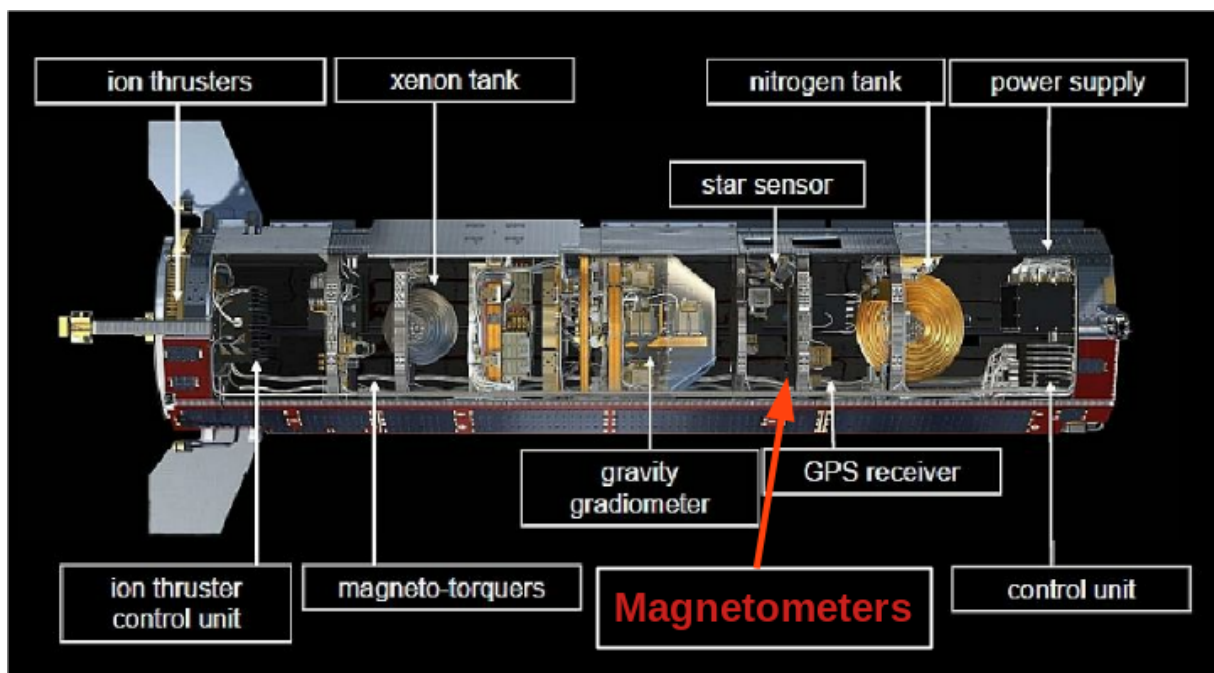


Figure 3. Location of instruments at the satellite body. (Credits: ESA)

are selected from the attitude dataset EGG\_IAQ\_li that are closest to MAG dataset timestamps. This subset of input data was used to interpolate all other data, that is position, magnetometer, magnetorquer, currents and other housekeeping (HK) data listed in Table 1. For each time of the combined dataset predictions of high-level geomagnetic field model for core, crustal and external contributions have been calculated from the CHAOS-7 magnetic field model following (Finlay et al. 2020). For the selection of the low-latitude range, we also calculate quasi-dipole latitude and MLT (Richmond 1995; Emmert et al. 2010) for each record. For selection of the geomagnetic quiet days, we use the geomagnetic Kp index (Matzka et al. 2021) and the geomagnetic equatorial Dst index (World Data Center for Geomagnetism 2015).

### Coordinate Frames

The Satellite Physical Coordinate Frame (SC\_O\_p), called SC in the following, is defined in Kolkmeier et al. (2008). The three MAGs are aligned with the principle axis of the satellite. The rotation of a vector in SC to MAG reference frame is given in Equation 1.

$$\overline{MAG_i} = \underline{R_{SC2MAG}} \overline{SC} \quad (1)$$

with

$$\underline{R_{SC2MAG}} = \begin{bmatrix} -1 & 0 & 0 \\ 0 & 1 & 0 \\ 0 & 0 & -1 \end{bmatrix} \quad (2)$$

That means negative  $\mathbf{MAG}_{i,x}$  is aligned with the flight-direction,  $\mathbf{MAG}_{i,z}$  points to the Earth and  $\mathbf{MAG}_{i,y}$  completes the orthogonal coordinate system.

The Gradiometer Reference Frame (GRF) is the coordinate system in which the measurements of GOCE's main instrument, the Electrostatic Gravity Gradiometer (EGG), are given. These are the gravity tensor and the combined STR and EGG attitude of the satellite with respect to the International Celestial Reference Frame (ICRF). GOCE provides a high quality attitude product, EGG\_IAQ\_li (Frommknecht et al. 2011), which is the combination of the star cameras and the Electrostatic Gravity Gradiometer (EGG). Fixed reference frames for all instruments are expected to be stable with respect to each other. Missing static rotations between reference frames will be corrected by Euler angle estimation during calibration.

Scientific evaluation of the data will be done in the Earth-fixed North-East-Centre (NEC) reference frame, which is the frame for CHAOS-7 prediction. The calibration and characterisation procedure has to be done in the same reference frame for measurements and model data. Calibration parameters are instrument

intrinsic and depend on the instrument reference frame. Characterisations of local disturbances are systematic in a local satellite reference frame. That leads to the decision to apply calibration and characterisation in the MAG reference frame.

For rotation of CHAOS-7 predictions,  $\mathbf{B}_{\text{model,NEC}}$ , from NEC to MAG reference frame a chain of rotations is needed. The first is the rotation from NEC to International Terrestrial Reference Frame (ITRF) depending on the latitude and longitude of the satellite location. We use Seeber (2003, page 23) to define a North-East-Zenith reference frame. By changing the sign of the z-direction (3rd row) we get a North-East-Centre reference frame, Equation 3.

$$\underline{R_{ITRF2NEC}} = \begin{vmatrix} -\sin(\Phi) \cdot \cos(\Lambda) & -\sin(\Phi) \cdot \sin(\Lambda) & \cos(\Phi) \\ -\sin(\Lambda) & \cos(\Lambda) & 0 \\ -\cos(\Phi) \cdot \cos(\Lambda) & -\cos(\Phi) \cdot \sin(\Lambda) & -\sin(\Phi) \end{vmatrix} \quad (3)$$

with latitude  $\Phi$  and longitude  $\Lambda$ .

The second is a rotation from ITRF to ICRF, taking into account Earth's nutation and precession.  $\underline{R_{ITRF2ICRF}}$  is calculated by application of the SOFA library function `iauC2t06a` (IAU SOFA Board 2019) and using Earth rotation parameters that are derived from the International Earth Rotation and Reference Systems service (IERS 2020).

The rotation from ICRF to GRF frame is given by quaternions available in the `EGG_GGT.li` product. GRF and SC reference frames are nominally parallel (Kolkmeier et al 2008), we can set the quaternions given in `EGG_GGT.li` product to derive the rotation from ICRF to SC,  $q_{ICRF2SC}$ .

Rotations can be combined very stably using quaternion algebra. Hence, we need to convert the direction cosine representation of  $\underline{R_{NEC2ITRF}}$ ,  $\underline{R_{ITRF2ICRF}}$  and  $\underline{R_{SC2MAG}}$  to a quaternion representation  $q_{NEC2ITRF}$ ,  $q_{ITRF2ICRF}$  and  $q_{SC2MAG}$  following (Wertz 1978, page 415). In summary, the complete rotation from the NEC to the MAG frame is given as

$$\mathbf{q}_{NEC2MAG} = \mathbf{q}_{NEC2ITRF} \cdot \mathbf{q}_{ITRF2ICRF} \cdot \mathbf{q}_{ICRF2SC} \cdot \mathbf{q}_{SC2MAG} \quad (4)$$

$$\mathbf{B}_{NEC} \xrightarrow{\mathbf{q}_{NEC2ITRF}} \mathbf{B}_{ITRF} \xrightarrow{\mathbf{q}_{ITRF2ICRF}} \mathbf{B}_{ICRF} \xrightarrow{\mathbf{q}_{ICRF2SC}} \mathbf{B}_{SC} \xrightarrow{\mathbf{q}_{SC2MAG}} \mathbf{B}_{MAG} \quad (5)$$

CHAOS-7 predictions are finally rotated from NEC to the MAG frame applying the rotation quaternion in Equation 4 following (Wertz 1978, page 759):

$$\mathbf{B}_{\text{model,MAG}} = \mathbf{q}_{NEC2MAG}^{-1} \cdot \mathbf{B}_{\text{model,NEC}} \cdot \mathbf{q}_{NEC2MAG} \quad (6)$$



For rotation of calibrated and characterised MAG data Equation 6 has to be applied in inverse order on  $\mathbf{B}_{\text{MAG}}$ .

### Pre-Processing

The three equal fluxgate magnetometers on the GOCE satellite are mounted perfectly aligned side-by-side with a distance of 80 mm. For that reason one would expect them to give the same results at the same times. However, when looking at the residuals of the individual components from different magnetometers, respectively, some large steps are visible. We found no correlation with activity of GOCE instruments or major events. We had to correct those events by hand before applying the calibration, and call this step block correction in the following. For each component of MAG2 and MAG3 we subtracted the corresponding component of MAG1. We identified timestamps of the beginning of each block correction by using a higher resolution figure of Figure 4. The first block has been set as reference for all components of MAG2 and MAG3. For all further blocks the offset of MAG2 and MAG3 has been corrected to reach the same mean value as the first block. At the end the mean value of all blocks has been removed from MAG2 and MAG3. After the block correction has been applied the residuals between the magnetometers look similar, as can be seen in Figure 4. Since there will be no relevant scientific output from three calibrated magnetometers very close to each other we decided to combine the three magnetometers into one single instrument by using the mean value, Equation 7:

$$\mathbf{B}_{\text{MAG}} = \frac{\sum_{i=1}^3 \mathbf{B}_{\text{MAG}i}}{3} \quad (7)$$

By combination of the three instruments we reduced the noise level of the input data and fill small gaps in single magnetometer records.

### Calibration and characterisation

Since the magnetometers of GOCE are used for the Drag-free Attitude and Orbit Control System (DFACS) they have been calibrated on-ground to fulfil the specification for DFACS which has biases of less than 500 nT. The pre-calibrated dataset is provided in the AUX\_NOM\_1B product. Previous studies, like Stolle et al. (2021) for GRACE-FO and Olsen et al. (2020) for CryoSat-2 showed that adding more internal features like currents, and temperatures that may cause perturbations can lead to much better calibrated datasets. We follow the same approach as Stolle et al. (2021) but adapt it to conditions and limitations of the GOCE satellite, e.g. availability of currents and temperatures.

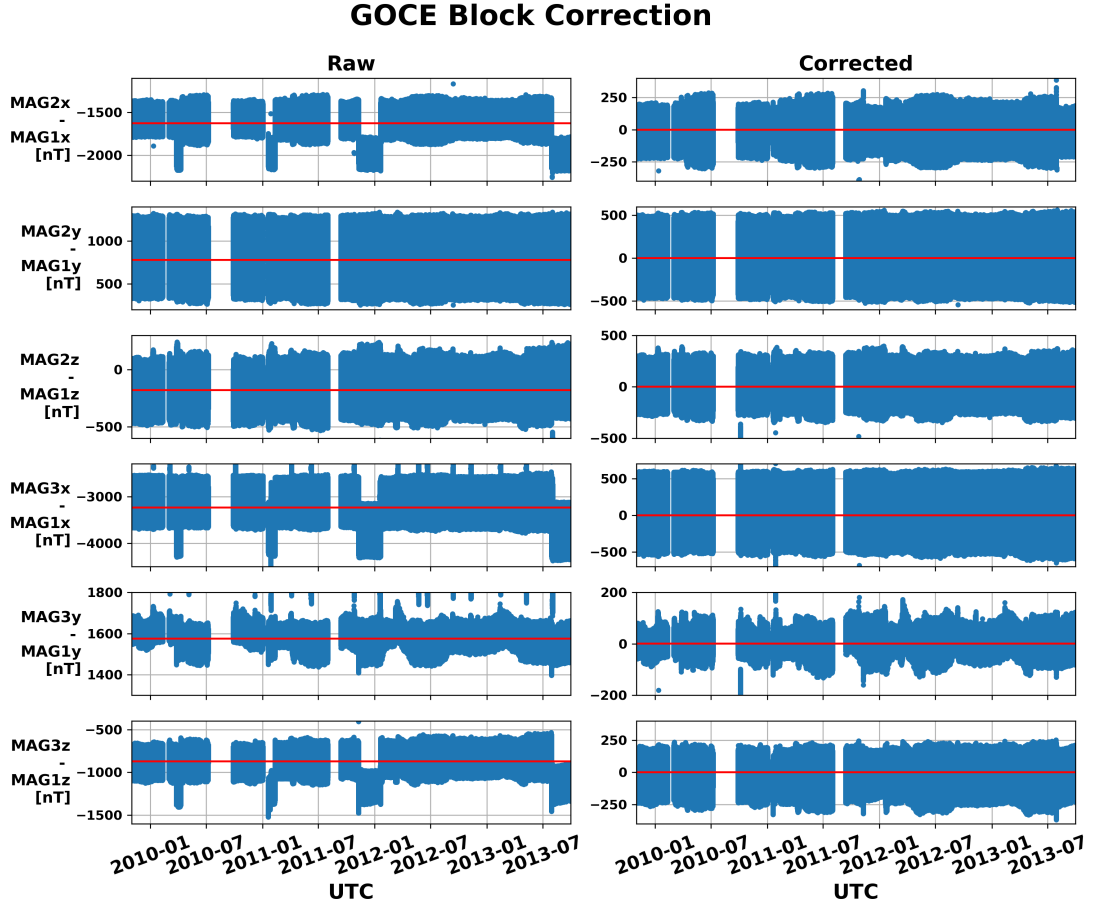


Figure 4. Overview of block correction for the whole mission. Shown are the differences between magnetometers 2 and 1, and 3 and 1 for the x, y, and z components from top to bottom. Without block-correction (left) and after applied block correction (right).



Calibration and characterisation will be applied on a subset only, to avoid that natural variations are interpreted as disturbances, but remain part of the data after the calibration procedure. Therefore we use only geomagnetic quiet times when natural variations should not be measured by the satellite, thus allowing for a post-launch calibration of the satellite system itself. Concretely, we use only data with  $|QDLAT| < 50^\circ$ ,  $Kp \leq 3$ ,  $|Dst| \leq 30$  nT and  $B\_Flag = 0$ .  $B\_Flag$  is a quality flag that gives non-zero values if the data gap for interpolation of input data is larger than 16 seconds. Since the resolution of the magnetometer data is only 16 seconds, we decided to use monthly data for the estimation of calibration and characterisation parameters. That avoids high fluctuation in estimated parameters but still gives a long term trend of parameter evolution with time to cope with system changes and deterioration. An ordinary least squares linear regression has been applied to estimate the parameters  $\mathbf{m}_{\text{cal}}$  and  $\mathbf{m}_{\text{char}}$  to optimise for  $S$ :

$$S = |(\mathbf{B}_{\text{cal}}(\mathbf{m}_{\text{cal}}, \mathbf{E}) + \mathbf{B}_{\text{char}}(\mathbf{m}_{\text{char}}, \mathbf{d}_{\text{char}})) - \mathbf{B}_{\text{model, MAG}}|^2 \quad (8)$$

with the calibrated magnetic field vector  $\mathbf{B}_{\text{cal}}$  using instrument-intrinsic calibration parameters,  $\mathbf{m}_{\text{cal}} = (\mathbf{b}, \mathbf{s}, \mathbf{u}, \mathbf{e}, \xi, \nu)$  that have been applied on the raw magnetic field vector  $\mathbf{E}$ , as given in Equation 12. For estimation of the characterised magnetic field vector  $\mathbf{B}_{\text{char}}$  characterisation parameters describing the impact on the housekeeping data  $\mathbf{m}_{\text{char}} = (\underline{M}, \underline{bat}, \underline{sa}, \underline{bt}, \underline{st}, \underline{hk})$  have been applied to the housekeeping data  $\mathbf{d}_{\text{char}} = (\mathbf{A}_{\text{MTQ}}, \mathbf{A}_{\text{BAT}}, \mathbf{A}_{\text{SA}}, \mathbf{A}_{\text{HK}}, \mathbf{T}_{\text{MAG}}, \mathbf{E}_{\text{st}})$ , as given in Equation 16.  $\mathbf{B}_{\text{model, MAG}}$  includes the CHAOS-7 magnetic field estimations for the core, crustal and large-scale magnetospheric field rotated into the instrument MAG frame as described by Equation 6.

From previous satellite missions like GRACE-FO it was known that additional time shifts between instrument measurements may occur. We repeated the calibration and characterisation procedure for a range of time shifts within an interval of  $\pm 2$  s in steps of 0.1 s on the most quiet data set, which was in December 2009. Best calibration results (minimum of the absolute values of residual to CHAOS-7) have been determined with a shift of 0.4 s for MAG data.

### Parameters for vector calibration

The previously combined magnetometer data act as the raw magnetic field vector for calibration, in MAG frame named  $\mathbf{E} = (E_1, E_2, E_3)^T$  in nT. The calibration estimates the nine instrument-intrinsic parameters scale factors  $\mathbf{s} = (s_1, s_2, s_3)^T$ , offsets  $\mathbf{b} = (b_1, b_2, b_3)^T$  and mis-alignment angles of the coil windings  $\mathbf{u} = (u_1, u_2, u_3)^T$ . Additionally, mis-alignment between static reference frames may occur, e.g.

due to slight rotation during mounting of instruments. This misalignment is estimated in a vector of Euler (1-2-3) angles  $\mathbf{e} = (e_1, e_2, e_3)^T$ , following Wertz (1978, page 764), or in a direction cosine rotation matrix,  $\underline{R}_A$ , which includes the three external parameters. Euler (1-2-3) represents three rotations about the first, second and third axis, in this order. The parameters are used to describe

$$\mathbf{B}_{\text{cal}} = \underline{R}_A \underline{P}^{-1} \underline{S}^{-1} (\mathbf{E} - \mathbf{b}) = \underline{A} (\mathbf{E} - \mathbf{b}) = \underline{A} \mathbf{E} - \mathbf{b}_A \quad (9)$$

where  $\underline{R}_A$  is the direction cosine matrix representation of the Euler (1-2-3) angles  $\mathbf{e}$ ,  $\underline{P}^{-1}$  is the misalignment angle lower triangular matrix

$$\underline{P}^{-1} = \begin{vmatrix} 1 & 0 & 0 \\ \frac{\sin(u_1)}{\cos(u_1)} & \frac{1}{\cos(u_1)} & 0 \\ -\frac{\sin(u_1)\sin(u_3)+\cos(u_1)\sin(u_2)}{w\cos(u_1)} & -\frac{\sin(u_3)}{w\cos(u_1)} & 1/w \end{vmatrix}$$

with:  $w = \sqrt{1 - \sin^2(u_2) - \sin^2(u_3)}$

(10)

and  $\underline{S}^{-1}$  is the diagonal matrix including the inverse of the scale factor

$$\underline{S}^{-1} = \begin{vmatrix} 1/s_1 & 0 & 0 \\ 0 & 1/s_2 & 0 \\ 0 & 0 & 1/s_3 \end{vmatrix} \quad (11)$$

Equation 9 is valid for fluxgate magnetometers treated as linear instruments. Brauer et al. (1997) showed that Equation 9 needs to be extended for non-linear effects of 2nd ( $\underline{\xi}$ ) and 3rd ( $\underline{\nu}$ ) order by 2nd ( $\mathbf{E}_\xi$ ) and 3rd ( $\mathbf{E}_\nu$ ) order data:

$$\mathbf{B}_{\text{cal}} = \underline{A} \mathbf{E} - \mathbf{b}_A + \underline{\xi} \mathbf{E}_\xi + \underline{\nu} \mathbf{E}_\nu \quad (12)$$

with non-linearity parameters of 2nd order

$$\underline{\xi} = \begin{vmatrix} \xi_{11}^1 & \xi_{22}^1 & \xi_{33}^1 & \xi_{12}^1 & \xi_{13}^1 & \xi_{23}^1 \\ \xi_{11}^2 & \xi_{22}^2 & \xi_{33}^2 & \xi_{12}^2 & \xi_{13}^2 & \xi_{23}^2 \\ \xi_{11}^3 & \xi_{22}^3 & \xi_{33}^3 & \xi_{12}^3 & \xi_{13}^3 & \xi_{23}^3 \end{vmatrix} \quad (13)$$

non-linearity parameters of 3rd order

$$\underline{\nu} = \begin{vmatrix} \nu_{111}^1 & \nu_{222}^1 & \nu_{333}^1 & \nu_{112}^1 & \nu_{113}^1 & \nu_{223}^1 & \nu_{122}^1 & \nu_{133}^1 & \nu_{233}^1 & \nu_{123}^1 \\ \nu_{111}^2 & \nu_{222}^2 & \nu_{333}^2 & \nu_{112}^2 & \nu_{113}^2 & \nu_{223}^2 & \nu_{122}^2 & \nu_{133}^2 & \nu_{233}^2 & \nu_{123}^2 \\ \nu_{111}^3 & \nu_{222}^3 & \nu_{333}^3 & \nu_{112}^3 & \nu_{113}^3 & \nu_{223}^3 & \nu_{122}^3 & \nu_{133}^3 & \nu_{233}^3 & \nu_{123}^3 \end{vmatrix} \quad (14)$$

and modulated data vectors of 2nd and 3rd order:

$$\mathbf{E}_\xi = (E_1^2, E_2^2, E_3^2, E_1 E_2, E_1 E_3, E_2 E_3)^T$$

$$\mathbf{E}_\nu = (E_1^3, E_2^3, E_3^3, E_1^2 E_2, E_1^2 E_3, E_2^2 E_3, E_1 E_2^2, E_1 E_3^2, E_2 E_3^2, E_1 E_2 E_3)^T \quad (15)$$

## Parameters for characterisation

Characterisation consists of the identification and, if possible, correction of artificial magnetic perturbations contained in the raw magnetic data. By simple correlation analysis combined with knowledge from former satellite missions like CHAMP, Swarm and GRACE-FO we identified the magnetorquer currents,  $\mathbf{A}_{\text{MTQ}}$ , the magnetometer temperature,  $\mathbf{T}_{\text{MAG}}$ , the battery currents,  $\mathbf{A}_{\text{BAT}}$ , the solar array panel currents,  $\mathbf{A}_{\text{SA}}$ , and a set of housekeeping currents, and temperatures  $\mathbf{A}_{\text{HK}}$ , to affect the GOCE magnetometer data. We also consider an effect from the correlation between the magnetometer temperature and magnetic field residuals,  $\mathbf{E}_{\text{st}} = \mathbf{E} \cdot (\mathbf{T}_{\text{MAG}} - T_0)$ , where  $T_0$  is the monthly median of  $\mathbf{T}_{\text{MAG}}$ . The characterisation equation is a combination of all identified disturbances:

$$\mathbf{B}_{\text{char}} = \underline{M} \cdot \mathbf{A}_{\text{MTQ}} + \underline{bat} \cdot \mathbf{A}_{\text{BAT}} + \underline{sa} \cdot \mathbf{A}_{\text{SA}} + \underline{hk} \cdot \mathbf{A}_{\text{HK}} + \underline{bt} \cdot (\mathbf{T}_{\text{MAG}} - T_0) + \underline{st} \cdot \mathbf{E}_{\text{st}} \quad (16)$$

Input data used in Equations 12 and 16 are listed in Tables 1 and 2, respectively. All input parameters and calibrated magnetic observation products are provided in CDF format, in the same format as for GRACE-FO (Michaelis et al. 2021).

## Results and Discussion

In this section, we discuss the final GOCE data set and some potential applications. We assess the residuals to CHAOS-7 predictions of all vector components and compare the lithospheric field measured from the GOCE data to the lithospheric field contribution included in CHAOS-7. Moreover, we calculate auroral field-aligned currents (FAC) and compare magnetospheric ring currents measured by GOCE with ground based estimations like the Geomagnetic Equatorial Disturbance Storm Time Index (Dst).

### Assessment of the final data set

To assess the temporal robustness of the calibration, time series of calibration parameters are shown in Figure 5 for offsets, scale factors, non-orthogonalities and Euler angles. Red lines show the average mean absolute deviation of the parameters. The parameters show no long-term trends over the mission duration. Comparisons with previously published studies gave similar order results for the mean absolute deviation of the parameter time series for CryoSat-2 (Olsen et al. 2020). However, in detail GOCE shows much higher variations in each of the parameters. That might be caused by higher air pressure at GOCE's low altitude and the drag-free attitude and orbit control system.

Residuals for the calibrated magnetic field vector have been calculated with respect to CHAOS-7

Table 2. Estimated calibration and characterisation parameters including units and dimensionality.

Parameter	Description	Unit	Dimension
<b>s</b>	Scale factors	$\frac{nT}{nT}$	3
<b>b</b>	Offsets	$nT$	3
<b>u</b>	Misalignment angles	rad	3
<b>e</b>	Euler (123) angles	rad	3
$\xi$	2nd order non-linearity	$\frac{nT}{nT^2}$	3x6
$\nu$	3rd order non-linearity	$\frac{nT}{nT^3}$	3x10
$\underline{bt}$	Temperature dependency of offsets b	$\frac{nT}{^\circ C}$	3x3
$\underline{st}$	Temperature dependency of scale factors s	$\frac{nT}{nT^\circ C}$	3x3
$\underline{bat}$	Battery current scale factor	$\frac{nT}{mA}$	3x4
$\underline{sa}$	Solar array current scale factor	$\frac{nT}{mA}$	3x2
$\underline{M}$	Magnetorquer current scale factor	$\frac{nT}{mA}$	3x3
$\underline{hk}$	Housekeeping data		3x25

predictions for geomagnetic quiet conditions and low latitudes, i.e.  $|QDLAT| < 50^\circ$ ,  $Kp \leq 3$ , and  
 $|Dst| \leq 30$  nT. Table 3 shows the mean and standard deviation of these residuals for the whole mission  
 period, and for the most quiet day in the most quiet month. The mean values are close to zero which  
 means that the calibration removed the offsets correctly. For very quiet conditions,  $Kp < 1$ , the standard  
 deviation can be reduced to values below 8 nT. The calibration has been applied on monthly data. Results  
 for the standard deviation of residuals with respect to the CHAOS-7 model are given for each month in  
 Table 4 for calibrated magnetometer data in MAG and NEC as well as for raw data of magnetometer  
 MAG<sub>1</sub> as representative example. The last three columns give the percentage of data used for the specific  
 month, the mean Kp value and mean Dst value from within data selection for the calibration. Standard  
 deviations vary strongly from month to month. For the majority of months the standard deviation is  
 reduced to the level of very quiet conditions. However, some months deviate strongly from the quiet days.  
 For some of those extreme months, a correlation with missing data or higher geomagnetic conditions seems  
 to exist. However, we cannot state a general correlation of high residuals with high activity. In general,  
 the values for mean and standard deviation have been significantly reduced by the calibration to values  
 between 7 and 13 nT, and are similar to residuals for GRACE-FO given by Stolle et al. (2021) and for  
 CryoSat-2 by Olsen et al. (2020), which varied between 3 nT and 10 nT (GRACE-FO) and 4 nT and  
 15 nT (CryoSat-2).

The estimation of impact for non-intrinsic instrument parameters is shown in Table 5. The impact has  
 been estimated by residual calculation between using all estimated parameters and using all but one  
 parameter and setting this one parameter to a neutral value. As an example, to estimate the impact of  
 $\Delta \mathbf{B}_{SA}$ , first all estimated parameters are applied to Equation 16 to compute  $\mathbf{B}_{char}$ . Then, the same  
 approach is repeated with  $\underline{sa}$  being set to zero and calculating  $\mathbf{B}_{char,zerosa}$ . The difference between  $\mathbf{B}_{char}$   
 and  $\mathbf{B}_{char,zerosa}$  is the impact of parameter  $\underline{sa}$ , called  $\Delta \mathbf{B}_{SA}$ . The results indicate that  $\underline{hk}$  and  $\underline{sa}$  have  
 the largest impact. On other missions, e.g. GRACE-FO (Stolle et al. 2021), an even larger standard  
 deviation of impact from solar panels than for the other parameters was found. The influence might be  
 smaller on GOCE due to design and orbit characteristics of the GOCE satellite. The solar arrays are  
 mounted such that they are always on the bright side with the GOCE dusk-dawn orbit, so that currents  
 induced by the solar arrays are more or less constant and do not vary much.

Figure 6a provides global maps of the residuals between the processed data and CHAOS-7 predictions  
 for December 2009 with the mean of the residuals summarised in bins of size of  $5^\circ$  geocentric latitude



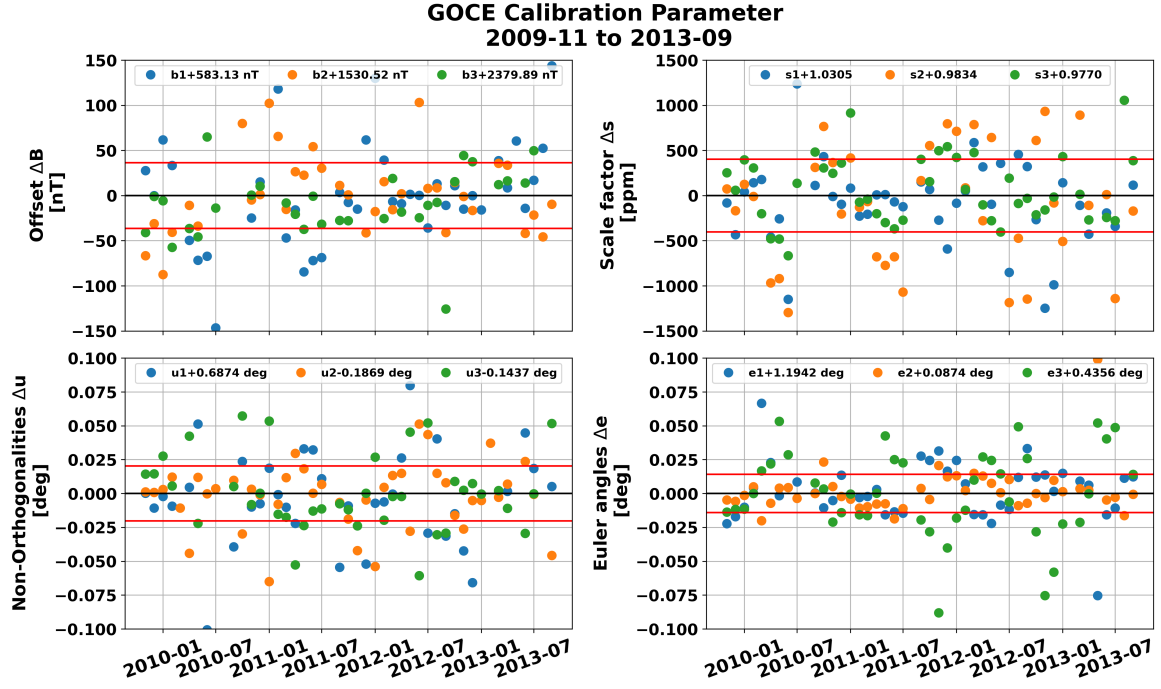


Figure 5. Time series of instrument-intrinsic calibration parameters offset (top-left), scale factors (top right), non-orthogonalities (bottom-left) and Euler angles (bottom-right) with respect to their median value. Red lines indicate average mean absolute deviation.

Table 3. Mean and standard deviation of residuals to CHAOS-7 for GOCE for geomagnetic quiet times and for a single quiet day, 2009-12-01.  $B_{MAG}$  and  $B_{NEC}$  represent residuals for calibrated data and  $B_{RAW}$  for data before calibration.

Parameter	Whole Period						Single Day					
	Mean [nT]			Std [nT]			Mean [nT]			Std [nT]		
	x	y	z	x	y	z	x	y	z	x	y	z
$\Delta B_{MAG}$	0.0	-0.1	-0.0	116.7	276.3	115.9	1.1	-1.6	0.4	8.3	6.1	5.6
$\Delta B_{NEC}$	-2.8	-0.1	-0.3	135.5	271.5	106.3	0.1	1.0	0.4	8.3	6.4	5.6
$\Delta B_{RAW1}$	-592.4	-1618.6	-2318.3	763.1	554.2	623.1	-549.1	-1587.2	-2269.3	752.9	495.4	594.3
$\Delta B_{RAW2}$	-597.3	-1613.6	-2311.7	796.1	743.2	695.9	-543.2	-1580.9	-2273.3	792.8	700.4	664.5
$\Delta B_{RAW3}$	-589.3	-1620.6	-2314.0	721.1	565.4	560.2	-531.7	-1595.6	-2285.6	712.0	502.3	517.1

Table 4. Standard deviation of residuals to CHAOS-7 for GOCE for all months in the mission period.

$\mathbf{B}_{\text{MAG}}$  and  $\mathbf{B}_{\text{NEC}}$  represent residuals for calibrated data and  $\mathbf{B}_{\text{RAW1}}$  for MAG<sub>1</sub> data before calibration.

The amount of data used for calibration and the averages of the two geomagnetic activity indices Kp and Dst are also given.

Month Month	$\Delta\mathbf{B}_{\text{MAG}}$			$\Delta\mathbf{B}_{\text{NEC}}$			$\Delta\mathbf{B}_{\text{RAW1}}$			Used Data [%]	$\overline{\text{Kp}}$	$\overline{\text{Dst}}$ [nT]
	x [nT]	y [nT]	z [nT]	x [nT]	y [nT]	z [nT]	x [nT]	y [nT]	z [nT]			
2009-11-01	8.8	6.4	5.5	8.7	6.4	5.5	737.1	468.5	603.0	54.0	0.62	-2.0
2009-12-01	8.9	6.4	5.9	8.9	6.4	5.9	736.4	473.9	607.1	51.7	0.46	4.0
2010-01-01	9.2	6.9	6.4	9.2	6.9	6.4	739.0	470.7	600.7	51.6	0.63	-2.0
2010-02-01	8.9	7.6	5.6	8.9	7.6	5.6	737.1	472.3	601.1	18.1	1.11	-8.0
2010-03-01	80.7	276.7	59.1	34.5	284.0	68.7	754.9	551.5	611.0	50.6	1.06	-5.0
2010-04-01	13.7	9.4	40.8	13.5	9.8	40.8	735.8	489.0	615.2	42.1	1.08	-12.0
2010-05-01	13.1	11.5	15.5	13.1	11.5	15.5	732.2	485.2	613.8	40.5	1.12	-7.0
2010-06-01	18.9	169.8	31.2	37.8	160.6	54.2	730.6	512.6	614.0	47.6	1.41	-9.0
2010-07-01	30.7	44.0	28.1	30.6	44.1	28.1	721.9	474.0	617.0	8.5	1.49	-12.0
2010-08-01	NaN	NaN	NaN	NaN	NaN	NaN	NaN	NaN	NaN	0.0	NaN	NaN
2010-09-01	14.9	17.3	15.9	13.6	18.3	15.9	750.8	473.8	595.0	5.9	1.13	-12.0
2010-10-01	14.9	9.2	40.3	14.8	9.4	40.3	746.5	470.8	593.7	48.2	1.05	-9.0
2010-11-01	9.1	7.1	5.9	9.1	7.1	5.9	745.6	470.4	607.9	52.4	1.03	-8.0
2010-12-01	9.8	7.7	6.1	9.8	7.8	6.1	743.2	476.3	611.3	50.8	0.8	-7.0
2011-01-01	15.3	10.0	28.5	15.8	9.2	28.5	758.8	467.7	592.8	20.8	0.92	-2.0
2011-02-01	9.6	7.4	12.0	9.5	7.4	12.0	739.0	476.4	614.9	46.6	1.02	-9.0
2011-03-01	9.4	7.5	6.1	9.3	7.6	6.1	734.9	479.4	606.3	44.4	1.07	-5.0
2011-04-01	10.5	9.1	8.8	10.5	9.2	8.7	755.5	481.7	603.0	41.9	1.13	-5.0
2011-05-01	11.9	10.0	12.0	11.9	10.0	12.0	737.5	477.9	604.9	46.4	1.29	-7.0
2011-06-01	13.7	12.4	16.8	13.8	12.4	16.8	741.9	486.0	606.1	45.5	1.52	-9.0
2011-07-01	13.4	11.7	15.6	13.5	11.7	15.6	737.5	485.5	606.2	47.3	1.59	-9.0
2011-08-01	3.5	2.0	5.4	3.6	1.9	5.4	780.0	394.5	525.7	0.1	1.71	-15.0
2011-09-01	9.2	8.9	6.4	9.0	9.0	6.4	750.1	478.4	591.5	20.3	1.09	-14.0
2011-10-01	9.8	8.6	6.6	9.7	8.7	6.5	753.9	476.8	603.6	44.7	1.09	-11.0
2011-11-01	31.4	202.6	53.2	45.3	200.5	50.9	763.4	516.9	612.1	49.0	0.9	-9.0
2011-12-01	10.5	9.2	8.9	10.4	9.3	8.9	762.6	467.5	597.6	54.8	0.92	-3.0
2012-01-01	13.2	9.8	30.8	13.1	10.1	30.7	773.6	473.3	621.9	43.6	1.25	-3.0
2012-02-01	9.8	8.2	6.3	9.8	8.3	6.3	736.1	478.8	603.1	45.7	1.46	-9.0
2012-03-01	10.4	10.9	7.7	10.4	10.9	7.7	748.9	476.1	594.1	24.6	1.42	-14.0
2012-04-01	10.7	8.6	7.1	10.6	8.7	7.1	745.7	476.3	600.2	42.7	1.35	-12.0
2012-05-01	12.6	12.8	14.2	12.6	12.8	14.2	747.8	482.0	603.1	48.9	1.27	-5.0
2012-06-01	34.7	156.2	42.2	25.2	160.8	29.5	759.5	513.1	607.7	33.6	1.3	-5.0
2012-07-01	16.4	12.9	26.1	16.3	12.9	26.2	736.9	486.5	601.5	38.1	1.72	-9.0
2012-08-01	11.6	9.6	8.9	11.5	9.7	8.9	739.2	475.7	605.9	49.3	1.4	-4.0
2012-09-01	12.0	10.6	8.6	12.1	10.6	8.6	766.6	483.3	605.6	45.4	1.22	-2.0
2012-10-01	10.0	9.0	6.8	9.9	9.1	6.8	757.5	486.0	611.7	38.9	0.93	-7.0
2012-11-01	10.8	9.0	7.3	10.8	9.0	7.3	767.9	484.0	620.4	45.4	0.98	-6.0
2012-12-01	10.1	8.5	6.9	10.1	8.5	6.9	749.7	477.0	619.9	55.6	0.78	8.0
2013-01-01	33.9	180.6	49.4	37.3	183.7	32.7	754.9	512.4	617.2	50.2	1.01	0.0
2013-02-01	757.7	1736.0	757.6	888.5	1697.6	689.6	1117.1	1815.9	971.8	44.0	1.3	-6.0
2013-03-01	10.0	8.6	6.6	9.9	8.7	6.6	758.8	477.1	604.0	39.8	1.18	-6.0
2013-04-01	10.6	9.1	8.0	10.6	9.1	8.0	755.2	485.3	598.0	53.4	1.06	-4.0
2013-05-01	208.8	646.2	129.0	192.9	652.6	120.1	813.0	806.5	616.8	26.4	1.25	-5.0
2013-06-01	14.1	12.7	16.8	14.1	12.7	16.8	756.1	493.5	604.6	39.1	1.34	-11.0
2013-07-01	15.9	13.2	32.4	15.9	13.2	32.4	759.2	492.1	603.9	41.8	1.27	-9.0
2013-08-01	107.8	130.6	121.6	108.4	131.1	120.6	808.4	504.6	595.9	45.1	1.34	-9.0
2013-09-01	10.8	9.6	7.5	10.6	9.7	7.5	772.9	477.4	586.6	51.7	1.16	-3.0

Table 5. Magnetic impact of calibration and characterisation respectively for each parameter given in Equation 16 and the non-linear parameters in Equation 12. Results are given in the MAG reference frame.

Parameter	Std [nT]			Min [nT]			Max [nT]		
	x	y	z	x	y	z	x	y	z
$\Delta \mathbf{B}_\xi$	67.8	141.2	67.5	-13448.9	-27276.5	-12631.9	12828.2	35776.8	21688.7
$\Delta \mathbf{B}_\nu$	48.0	82.4	42.8	-11447.7	-20148.4	-10435.0	3830.4	10720.9	9133.3
$\Delta \mathbf{B}_{\text{MTQ}}$	56.6	33.6	29.3	-298.2	-705.7	-390.5	451.4	704.7	234.8
$\Delta \mathbf{B}_{\text{BAT}}$	33.4	93.3	48.4	-634.0	-725.3	-744.5	430.9	1225.6	1022.1
$\Delta \mathbf{B}_{\text{SA}}$	123.6	156.1	185.4	-885.4	-573.2	-784.2	814.0	1630.7	974.0
$\Delta \mathbf{B}_{\text{HK}}$	212.1	271.1	484.0	-1049.1	-1939.5	-2453.0	2985.5	1502.7	2469.2
$\Delta \mathbf{B}_{\text{BT}}$	12.4	4.4	43.9	-93.4	-128.3	-329.4	213.3	57.6	289.0
$\Delta \mathbf{B}_{\text{ST}}$	7.3	7.2	7.4	-387.7	-550.9	-347.5	307.4	340.0	400.9
$\Delta \mathbf{B}_{\text{cal,NEC}}$	135.5	271.5	106.3	-28906.3	-25670.8	-10717.4	10169.4	21387.6	32442.4

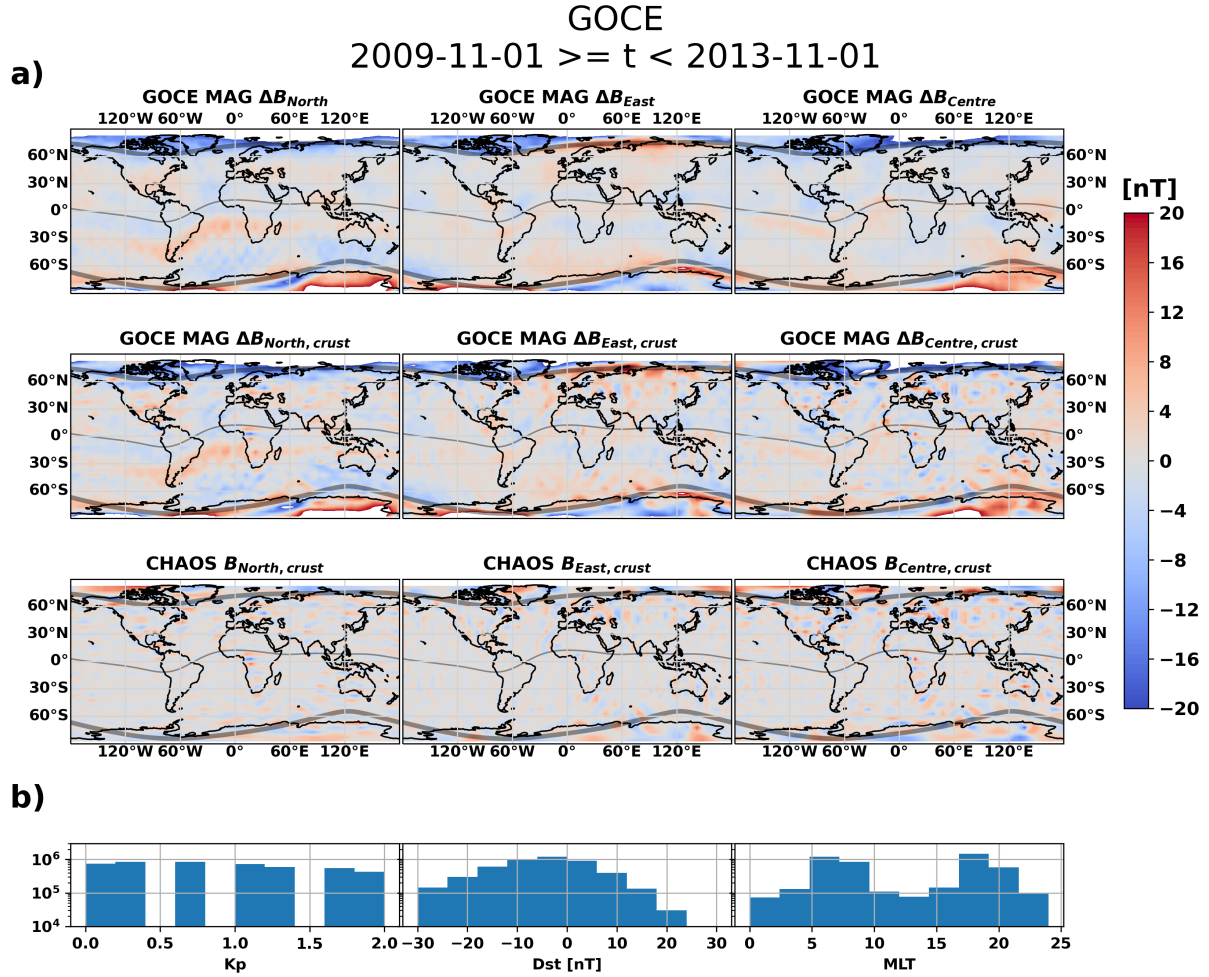


Figure 6. Top panel of a) shows magnetic residuals to CHAOS-7 (core, crustal and large-scale magnetospheric field). Middle panel of a): Magnetic residuals to CHAOS-7 (core and large-scale magnetospheric field). Bottom panel of a): Crustal field from CHAOS-7 model. The columns show the three NEC components North, East and Centre. b) shows the distribution of geomagnetic and solar activity indices and magnetic local time for data selection used in a).

and  $5^\circ$  geocentric longitude. The three columns represent the  $B_N$ ,  $B_E$  and  $B_C$  components of the NEC frame, respectively. The first row displays residuals to the core, the crustal and the large-scale magnetospheric field predictions of CHAOS-7. The second row shows residuals to only the core and the large-scale magnetospheric field predictions, i.e., in particular the lithospheric field is now included in the data. The third row shows the crustal field prediction from CHAOS-7. The grey lines indicate  $0^\circ$  and  $\pm 70^\circ$  magnetic latitude (QDLAT). Figure 6b) gives distribution of geomagnetic and solar indices and magnetic local time of the data set of this month, which was geomagnetically quiet. Auroral electrojet and field-aligned currents at high latitudes produce the largest deviations as they are measured by the satellite but not included in the CHAOS-7 model. Since the data is collected at a dawn-dusk orbit, no significant low and mid latitude ionospheric disturbances are expected, nor significant effects from magnetospheric currents during the quiet times. Still, there are systematic deviations that follow the geomagnetic equator in all components, and these are already known from GRACE-FO carrying the same type of magnetometers. However, besides the prominent disturbance at the geomagnetic equator there are large areas with absolute residuals below 4 nT as indicated by greyish colours. The comparison of second and third row of Fig. 6a also shows that the calibrated GOCE data can reproduce the large-scale crustal anomalies quite well. For example, the Bangui and Kursk anomaly in central Africa and Russia, respectively, are clearly seen. Still, a systematic artificial field with low amplitude along the geomagnetic equator is visible.

### Large-scale field-aligned currents

Field-aligned currents (FAC) are not part of the CHAOS7 model and should be kept in the measured data after calibration and characterisation. Since platform magnetometers have a higher noise level than science magnetometers, we expect only large-scale auroral field-aligned currents to be visible. Figure 7 shows results for FACs derived from GOCE MAG on the Northern (top) and Southern (bottom) hemisphere, selected for the northward (left) and southward (right) z-component of interplanetary magnetic field (IMF). Region 1 and 2 currents are prominently visible, similar to results from the PlatMag feasibility study for Swarm and GOCE [https://www.esa.int/Enabling\\_Support/Preparing\\_for\\_the\\_Future/Discovery\\_and\\_Preparation/ESA\\_s\\_unexpected\\_fleet\\_of\\_space\\_weather\\_monitors](https://www.esa.int/Enabling_Support/Preparing_for_the_Future/Discovery_and_Preparation/ESA_s_unexpected_fleet_of_space_weather_monitors).

### The magnetic effect of the magnetospheric ring current during the March 17, 2013 storm

A geomagnetic storm with values of  $Dst < -130$  nT occurred on March 17, 2013, Figure 8. The circles represent medians of residuals of the horizontal component of the magnetic field ( $\sqrt{B_N^2 + B_E^2}$ ) within

**GOCE MAG FAC**  
**2009-11-01T00:49:39.411000 - 2013-09-30T02:47:11.586000**  
**MLT vs QD LAT**

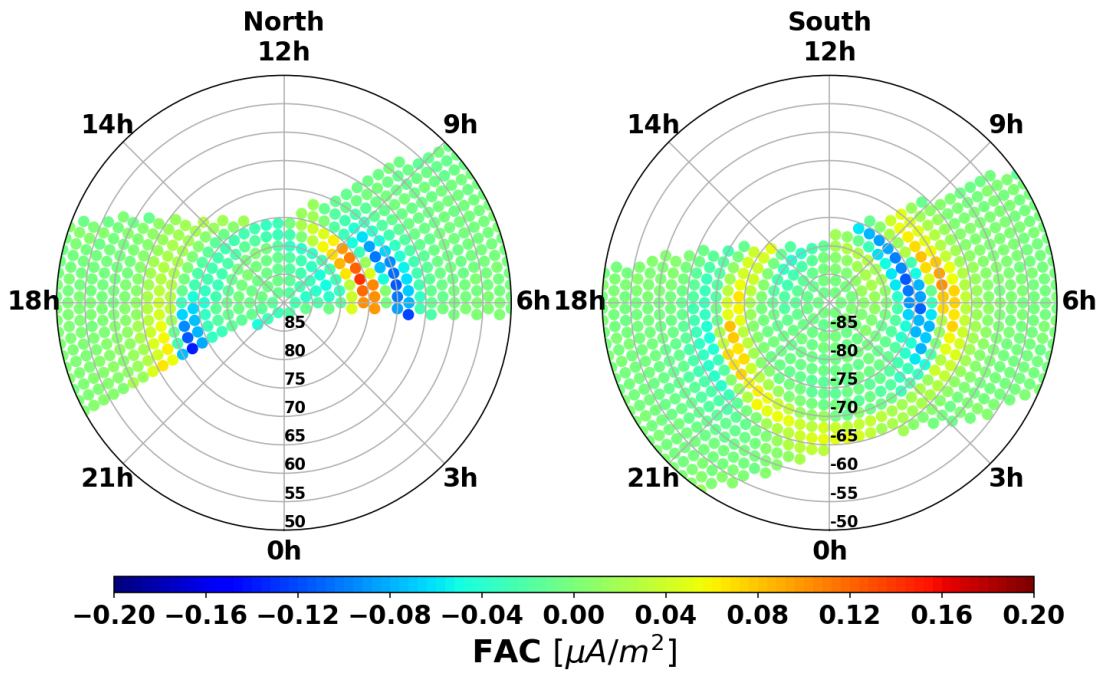


Figure 7. Quasi-dipole latitude (QDLAT) versus magnetic local time (MLT) large-scale field-aligned currents for the whole mission duration. The left panel shows the northern hemisphere and the right panel the southern hemisphere.

$\pm 10^\circ$  QDLAT and projected to  $0^\circ$  QDLAT for each low latitude orbital segment for ascending (blue) and descending (orange) orbits. The residuals are calculated with respect to the CHAOS-7 core and crustal field predictions. The large-scale magnetospheric field was not subtracted, and signatures from magnetospheric currents (including their induced counterparts in the Earth) remain included in the data. The ascending and descending orbit data generally agree well with each other and with the Dst index, despite the different retrieval technique for magnetospheric signatures in ground and satellite data. It is known from earlier studies that ground-based derived ring current signatures show systematic differences to those derived in space and that in particular the Dst index does not have the correct magnetospheric baseline (Maus and Lühr 2005; Olsen et al. 2005; Lühr et al. 2017; Pick et al. 2019). The ring current signal obtained from LEO satellites is generally lower than from ground, which is also reflected in an offset between the Dst index and the satellite derived residuals. In detail the ring current at ascending (MLT 6) nodes shows systematic weaker residual than for descending (MLT 18) nodes. That agrees well with dawn-dusk asymmetries found in studies from Newell and Gjerloev (2012) for Super MAG Ring current and Love and Gannon (2009) for Dst.

## **Conclusions**

The GOCE mission carries three vector magnetometers for attitude and orbit control. We applied a calibration and characterisation procedure that significantly reduces perturbations produced artificially by the satellite itself. The calibrated data from non-dedicated magnetometers in LEO can be used to fill gaps between dedicated magnetic field missions and in the MLT distribution. However, since non-dedicated missions do not carry an absolute magnetometer as reference, a high-level geomagnetic model based on dedicated missions is still needed for the calibration. Although calibrated platform magnetometer data cannot reach residuals below 1 nT to high-level geomagnetic models as dedicated mission data from, e.g., CHAMP and Swarm do, we have shown that they contain information about lithospheric and magnetospheric field signatures and of field-aligned currents. With standard deviations of residuals between 7 nT and 13 nT for quiet times our GOCE results are of similar order to those of CryoSat-2 and GRACE-FO calibrated magnetometer data (Olsen et al. 2020; Stolle et al. 2021). For a mission not dedicated to magnetic field research and not carrying scientific magnetometers, residuals in this order of magnitude are acceptable. The calibrated GOCE data are freely available and may be used for studying different magnetic field sources and the near-Earth space environment.

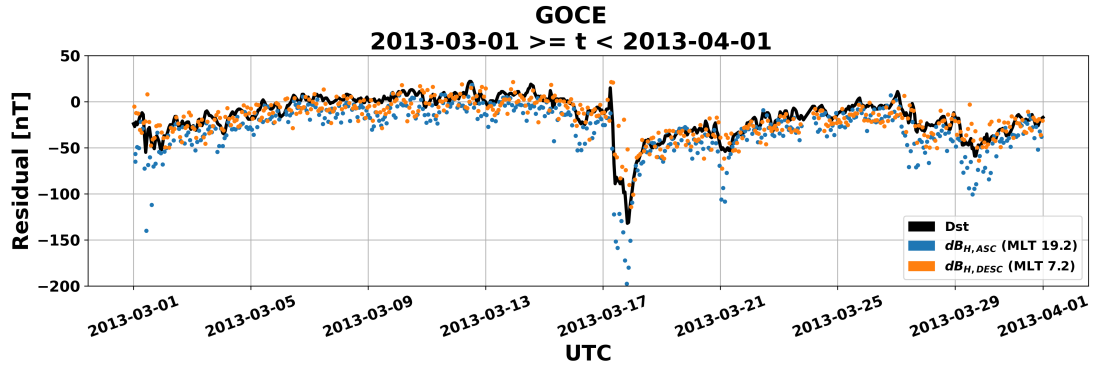


Figure 8. Time series of residuals of calibrated GOCE magnetic data to the core and crustal field of CHAOS-7 around the magnetic storm in March 2013. Ascending (ASC) nodes are plotted in blue, descending (DESC) nodes in orange. The Dst index is also plotted in black.



## List of abbreviations

CHAMP: CHALLENGING Minisatellite Payload; CHAOS: CHamp Ørsted SAC-C magnetic field model; CDF: Common Data Format; DFACS: Drag-free Attitude and Orbit Control System; Dst: Geomagnetic Equatorial Disturbance Storm Time Index; ESA: European Space Agency; FAC: Field-Aligned Currents; GFZ: Helmholtz Centre Potsdam, German Research Centre for Geosciences; GOCE: Gravity field and steady-state Ocean Circulation Explorer; GRACE-FO: Gravity Recovery and Climate Experiment Follow-On; GRF: Gradiometer Reference Frame; HK: Housekeeping; ICRF: International Celestial Reference Frame; IGRF: International Geomagnetic Reference Field IGRF-13; ISDC: Information System and Data Center at GFZ; ITRF: International Terrestrial Reference Frame; L1b: GOCE Level 1b data; LEO: Low Earth Orbit; MAG: Magnetometer; MLAT: Modified Apex Latitude; MLT: Magnetic Local Time; MTQ: Magnetorquer; NEC: North, East, Center coordinate system; PlatMag: Platform Magnetometer; QDLAT: Quasi-dipole latitude; SC: Spacecraft Physical Reference Frame; STR: Star cameras (Star TRackers)

## Acknowledgments

The European Space Agency (ESA) is gratefully acknowledged for providing the GOCE data. Special thanks to Björn Frommknecht (ESA) for pre-selection of housekeeping data. Kp is provided by GFZ, the Dst and AE indices by the Geomagnetic World Data Centre Kyoto, and F10.7 by the Dominion Radio Astrophysical Observatory and Natural Resources Canada. We thank Martin Rother (GFZ) for fruitful discussions.

## Authors' contributions

IM and CS defined the study. IM pre-processed and calibrated the data. JR derived FACs. CS, MK, IM, KSR analysed and interpreted the results. IM wrote the manuscript. All authors read and approved the final manuscript.

## Funding

This study has been partly supported by Swarm DISC activities funded by ESA under contract no. 4000109587/13/I-NB. KSR is supported through HEIBRIDS - Helmholtz Einstein International Berlin Research School in Data Science under contract no. HIDSS-0001.

## Availability of data and materials

The data generated and analysed in this paper is available at (Michaelis et al. 2022)  
[ftp://isdcdftp.gfz-potsdam.de/platmag/MAGNETIC\\_FIELD/GOCE/Analytical/v0205/](ftp://isdcdftp.gfz-potsdam.de/platmag/MAGNETIC_FIELD/GOCE/Analytical/v0205/).

## Competing interests

The authors declare that they have no competing interests.

## References

- Billingsley (2020). Billingsley TFM100SH Magnetometer.  
<https://magnetometer.com/products/fluxgate-magnetometers/tfm100s>,  
<https://magnetometer.com/wp-content/uploads/magnetometer-comaparison.pdf>,  
<https://magnetometer.com/wp-content/uploads/TFM100S-Spec-Sheet-February-2008.pdf>.
- Brauer P, Merayo J M G, Nielsen O V, Primdahl F, Petersen J R (1997). Transverse field effect in fluxgate sensors. *Sensors and Actuators A: Physical*, 59:70–74. ISSN 0924-4247.  
doi:10.1016/s0924-4247(97)01416-7.
- CHAMP: overview of final ME products and format description (2019) CHAMP Satellite Mission. *GFZ German Research Centre for Geosciences*, Scientific Technical Report STR - Data ; 19/10), (2019).  
doi:10.2312/GFZ.b103-19104.
- Emmert J T, Richmond A D, Drob D P (2010). A computationally compact representation of Magnetic Apex and Quasi-Dipole coordinates with smooth base vectors. *Journal of Geophysical Research*, 115:A08322. doi:10.1029/2010JA015326.
- Finlay C, Kloss C, Olsen N, M H, Tøffner-Clausen L, Grayver A, Kuvshinov A (2020). The CHAOS-7 geomagnetic field model and observed changes in the South Atlantic Anomaly. *Earth Planets Space*, 72:156. doi:10.1186/s40623-020-01252-9.
- Floberghagen R, Drinkwater M Haagmans R, Kern M (2008). GOCE’s Measurements of the Gravity Field and Beyond. *ESA Bulletin 133*.  
[https://www.esa.int/About\\_Us/ESA\\_Publications/ESA\\_i\\_Bulletin\\_i\\_133\\_February\\_2008g](https://www.esa.int/About_Us/ESA_Publications/ESA_i_Bulletin_i_133_February_2008g).
- Floberghagen R, Fehringer M, Lamarre D, Muzi d, Frommknecht b, Steiger C, Piñeiro J, and da Costa A (2011). Mission design, operation and exploitation of the Gravity field and steady-state Ocean Circulation Explorer mission. *Journal of Geodesy*, 85(11), 749-75. doi:10.1007/s00190-011-0498-3.

382 Frommknecht B, Lamarre D, Meloni M, Bigazzi A, Floberghagen R (2011). GOCE level 1b data  
 383 processing. *J Geod* 85:759-775. doi:10.1007/s00190-011-0497-4.  
 384 GOCE Flight Control Team (2014). GOCE End-of-mission operations report. Technical report  
 385 GO-RP-ESC-FS-6268, Issue 1, Revision 0.  
 386 <https://earth.esa.int/documents/10174/85857/2014-GOCE-Flight-Control-Team.pdf>.  
 387 IAU SOFA Board (2019). IAU SOFA Software Collection. <http://www.iausofa.org>.  
 388 IERS (2020). International Earth rotation and Reference systems Service (IERS) Earth Orientation  
 389 Center, Bulletin B. [ftp://hpiers.obspm.fr/eop-pc/bul/bulb\\_new](ftp://hpiers.obspm.fr/eop-pc/bul/bulb_new).  
 390 Kolkmeier A, Präger G, Möller P, Strandberg T, Kempkens K, Stark J, Gessler L, and Hienerwadel K  
 391 (2008). GOCE - DFAC Interface Control Document, Tech. Rep. GO-IC-ASG-0005\_12, EADS  
 392 Astrium.  
 393 Love J J, Gannon J L (2009). Revised  $D_{st}$  and the epicycles of magnetic disturbance: 1958–2007.  
 394 *Annales Geophysicae*, 27(8):3101–3131. doi:10.5194/angeo-27-3101-2009.  
 395 Lühr H, Xiong C, Olsen N, Le G (2017). Near-Earth Magnetic Field Effects of Large-Scale  
 396 Magnetospheric Currents. *Space Science Reviews*, 206:521–545. doi:10.1007/s11214-016-0267-y.  
 397 Matzka J, Bronkalla O, Tornow K, Elger K, Stolle C (2021). Geomagnetic Kp index. V. 1.0. GFZ Data  
 398 Services. doi:10.5880/Kp.0001.  
 399 Maus S, Lühr H (2005). Signature of the quiet-time magnetospheric magnetic field and its  
 400 electromagnetic induction in the rotating Earth. *Geophysical Journal International*, 162:755–763.  
 401 doi:10.1111/j.1365-246X.2005.02691.x.  
 402 Michaelis I, Stolle C, Rother M (2021). GRACE-FO calibrated and characterized magnetometer data..  
 403 *GFZ Data Services*. doi:10.5880/GFZ.2.3.2021.002.  
 404 Michaelis I, Korte M (2022). GOCE calibrated and characterised magnetometer data. *GFZ Data*  
 405 *Services*. doi:10.5880/GFZ.2.3.2022.001.  
 406 Newell P T, Gjerloev J W (2012). SuperMAG-based partial ring current indices. *Journal of Geophysical*  
 407 *Research*, 117:A05215. doi:10.1029/2012JA017586.  
 408 Olsen N, Sabaka T, Lowes F (2005). New parameterization of external and induced fields in  
 409 geomagnetic field modeling, and a candidate model for IGRF 2005. *Earth Planets Space*,  
 410 57(12):1141–1149. ISSN 1343-8832.  
 411 Olsen N, Friis-Christensen E, Floberghagen R, Alken P, Beggan CD, Chulliat A, Doornbos E, Da

Encarnaç o JT, Hamilton B, Hulot G, Van Den Ijssel J, Kuvshinov A, Lesur V, L hr H, Macmillan S, Maus S, Noja M, Olsen PEH, Park J, Plank G, P the C, Rauberg J, Ritter P, Rother M, Sabaka TJ, Schachtschneider R, Sirol O, Stolle C, Th bault E, Thomson AWP, T ffner-Clausen L, Vel msk  J, Vigneron P, Visser PN (2013) The Swarm Satellite Constellation Application and Research Facility (SCARF) and Swarm data products. *Earth, Planets and Space*, Vol. 65, pp. 1189-1200. doi:10.5047/eps.2013.07.001.

Olsen N (2021). Magnetometer Data of the GRACE Satellite Duo. *Earth Planets Space*, 73:62. doi:10.1186/s40623-021-01373-9.

Olsen N, Albini G, Bouffard J, Parrinello T, T ffner-Clausen L (2020). Magnetic observations from CryoSat-2: calibration and processing of satellite platform magnetometer data. *Earth Planets Space*, 72:48. ISSN 1880-5981. doi:10.1186/s40623-020-01171-9.

Pick L, Korte M, Thomas Y, Krivova N., Wu C.-J.(2019). Evolution of large-scale magnetic fields from near-Earth space during the last 11 solar cycles. *Journal of Geophysical Research: Space Physics*, 10.1029/2018JA026185,2527-2540. doi:10.1029/2018JA026185.

Richmond A (1995). Ionospheric electrodynamics using magnetic apex coordinates. *Journal of Geomagnetism and Geoelectricity*, 47:191–212. doi:10.5636/jgg.47.191.

Seeber G, editor (2003). *Satellite Geodesy, 2nd completely revised and extended edition*. Walter de Gruyter,Berlin,New York. ISBN 3-11-017549-5.

Stolle C, Michaelis I, Xiong C, Rother M, Usbeck T, Yamazaki Y, Rauberg J, Styp-Rekowski KM (2021). Observing Earth’s magnetic environment with the GRACE-FO mission.. *Earth Planets Space*, 73:51. doi:10.1186/s40623-021-01364-w.

Swarm DISC (2022). Swarm DISC (Swarm Data, Innovation, and Science Cluster). <https://earth.esa.int/eogateway/activities/swarm-disc>.

Wertz J R, editor (1978). *Spacecraft Attitude Determination and Control*, volume 73. Springer Netherlands. ISBN 978-90-277-1204-2. doi:10.1007/978-94-009-9907-7.

Nose M, Iyemori T, Sugiura M, Kamei T (2015). Geomagnetic Dst index. doi:10.17593/14515-74000.